Supplemental Information

Enzyme-inhibitor-like tuning of Ca^{2+} channel connectivity with calmodulin

Xiaodong Liu, Philemon S. Yang, Wanjun Yang, David T. Yue (2010) *Nature* **in press**

1. Additional data for Fig. 1

1.1. Detailed specification of constructs

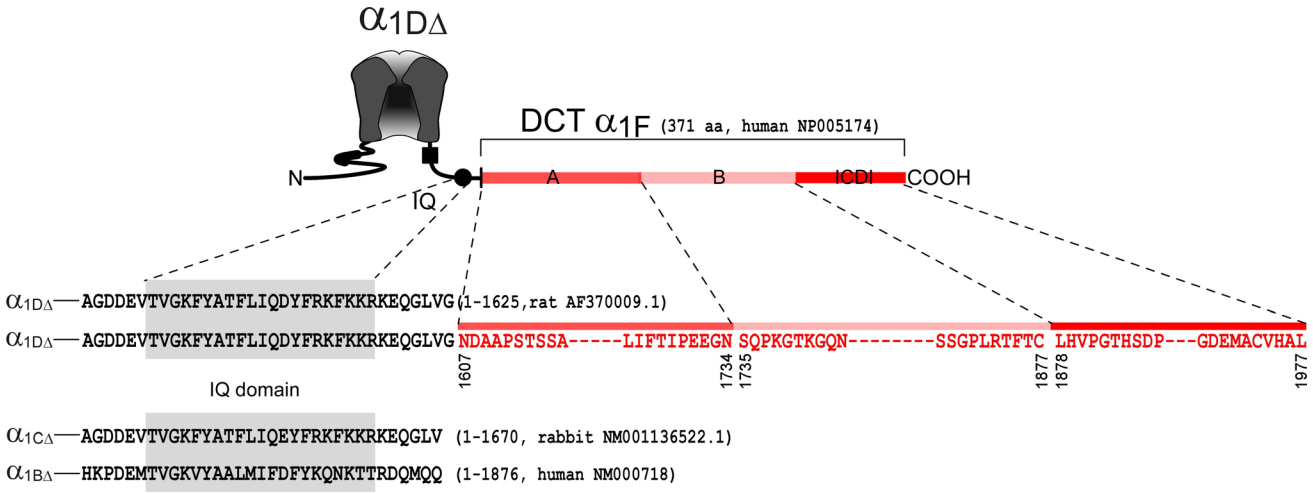

Fig. S1.1 Detailed sequence information for constructs used in Fig. 1, and affiliated supplemental information. In addition to α_1 subunits, we co-transfected auxiliary β_{2a} (M80545) and $\alpha_2\delta$ (NM012919.2) subunits throughout. Versions of $\alpha_{1C\Delta}$ and $\alpha_{1B\Delta}$ were appended to the DCT of α_{1F} as well. Accession numbers in parentheses. The DCT region was cloned non-directionally via a unique Xba I site, introducing an SR.

1.2. $Ca_V1.2$ channel CDI is decreased by the DCT of α_{1F}

Adding the $Ca_V1.4$ DCT to the $Ca_V1.2$ channel core (Figs. S1.2) also attenuated CDI. Panel **a** shows the CDI profile of the core $Ca_V1.2$ channel (Fig. S1.1 details the composition), with the display format identical to that in main text Fig. 1, except that reference depolarizations are to +10 mV, and bar graphs report the population data for inactivation metrics. Panel **b** displays the decrease, but not elimination of CDI seen upon addition of the DCT.

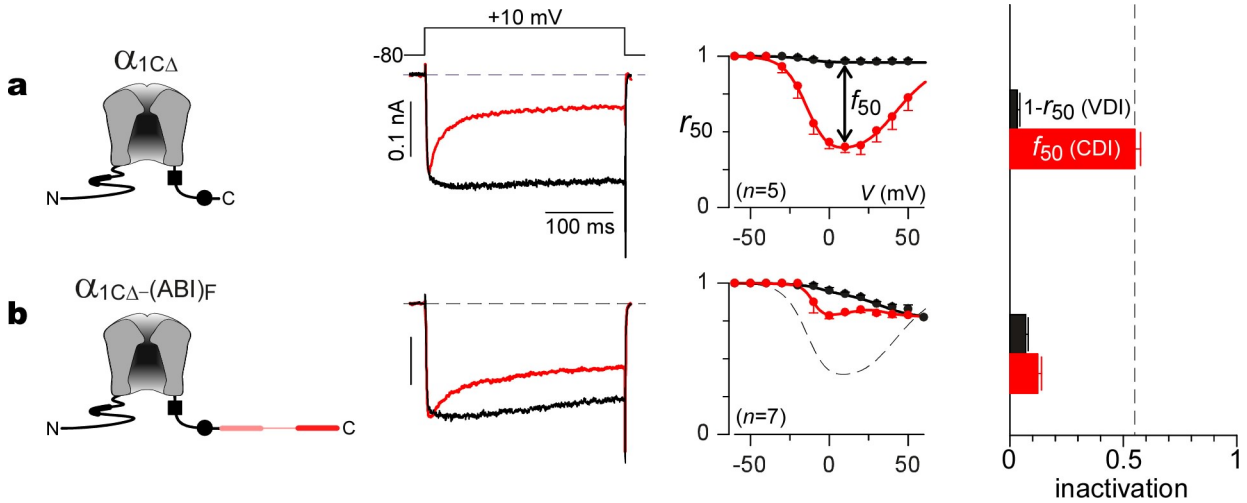

Fig. S1.2 Effects of the DCT of α_{1F} upon CDI in $Ca_V1.2$ channels. **a**, Behavior of core $Ca_V1.2$ channels. **b**, DCT of α_{1F} attenuates CDI of $Ca_V1.2$. Dashes reproduce Ca^{2+} profile from panel **a**. **a** and **b**, Format as in main text Fig. 1, except exemplar currents at 10 mV. Red bars show f_{50} values. Black bars show 1-r_{50} values for Ba^{2+} current.

1.3. $Ca_V2.2$ channel CDI is unaffected by the DCT of α_{1F}

By contrast to experiments with core channels comprised of Ca_V1 subunits (main text Fig. 1, Supplemental Fig. S1.2), appending the DCT of α_{1F} does *not* diminish CDI of core channels comprised of the main $Ca_V2.2$ subunit (α_{1B}). Fig. S1.3a summarizes the baseline CaM-mediated CDI of a core $Ca_V2.2$ channel[5], which incorporates the pore-forming $\alpha_{1B\Delta}$ subunit (defined above in Fig. S1.1). The format is identical to that in main text Fig. 1, except that 300-msec metrics are used to accommodate the slower CDI kinetics typical of these channels. Fig. S1.3b demonstrates that CDI is no different upon appending the DCT of α_{1F}. Thus, the DCT of α_{1F} requires complementary elements within the channel core, in order to reduce CDI. Those elements are presumably lacking in the $Ca_V2.2$ core.

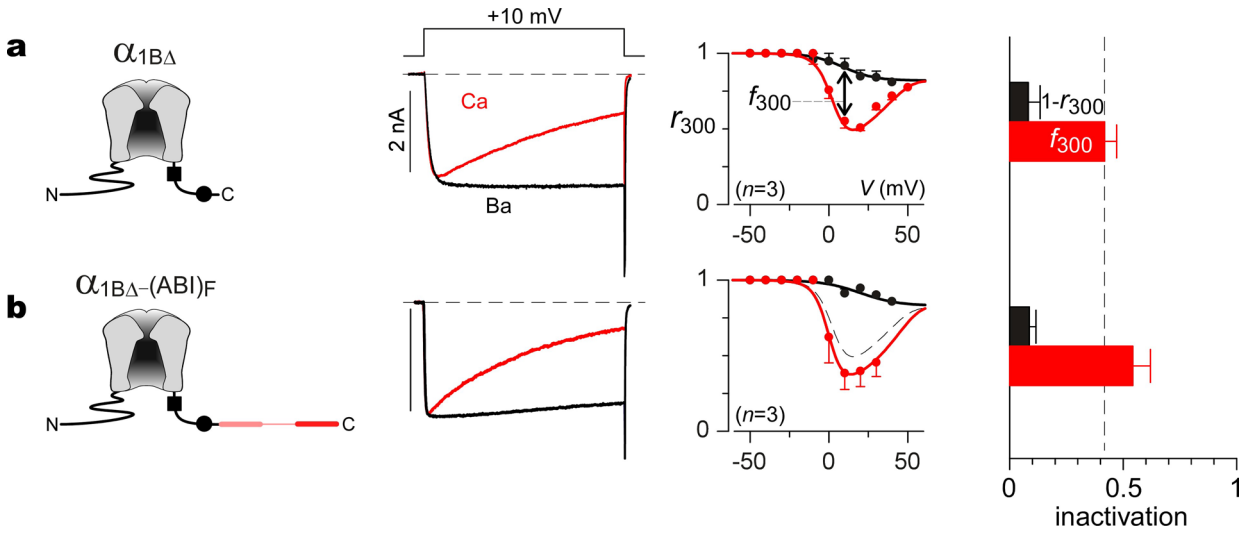

Fig. S1.3 DCT of α_{1F} does not diminish CDI of core channels comprised of the $Ca_V2.2$ pore-forming subunit ($\alpha_{1B\Delta}$). **a**, Baseline CDI. **b**, CDI upon appending the DCT of α_{1F}. Control metrics from **a** reproduced for reference. Patch solutions identical to those used for $Ca_V1.3$, except internal Ca^{2+} buffering now 0.5 mM EGTA, to allow for global Ca^{2+} selectivity of CDI within $Ca_V2.2$ channels[2]. Sequences as in Fig. S1.1.

1.4. Segment A and ICDI module of DCT of α_{1F} are functionally critical

To establish which elements within the DCT of α_{1F} were functionally critical for the attenuation of CDI, we performed additional deletion analysis of the $\alpha_{1D\Delta}$-$(ABI)_F$ construct in main text Fig. 1b. Fig. S1.4 summarizes the results, following the identical format to main text Fig. 1b, the average results of which are reproduced at the top for reference. Deleting the A region from the DCT rendered this module incapable of attenuating CDI (Fig. S1.4b); hence, the A segment is functionally critical. By contrast, deleting the B region from the DCT fully spared the module's ability to blunt CDI, yielding CDI attenuation equal to that seen with the entire DCT (Fig. S1.4c). Hence, the B region is functionally irrelevant. Deleting both A and B regions, leaving only the ICDI region, rendered the DCT module largely inactive (Fig. S1.4d), sparing a small decrement of CDI compared to core channels. Thus, while the ICDI element alone is capable of some effect, it requires the A segment for full activity. Finally, truncating the first 40 residues from the ICDI element in the $\alpha_{1D\Delta}$-$(AI)_F$ construct of Fig. S1.4c, entirely eliminates the DCT effect in the $\alpha_{1D\Delta}$-$(AI_{41\text{-}100})_F$ construct in Fig. S14e. Hence, at least part of the ICDI is critical. In all, both A and ICDI elements are necessary for DCT function.

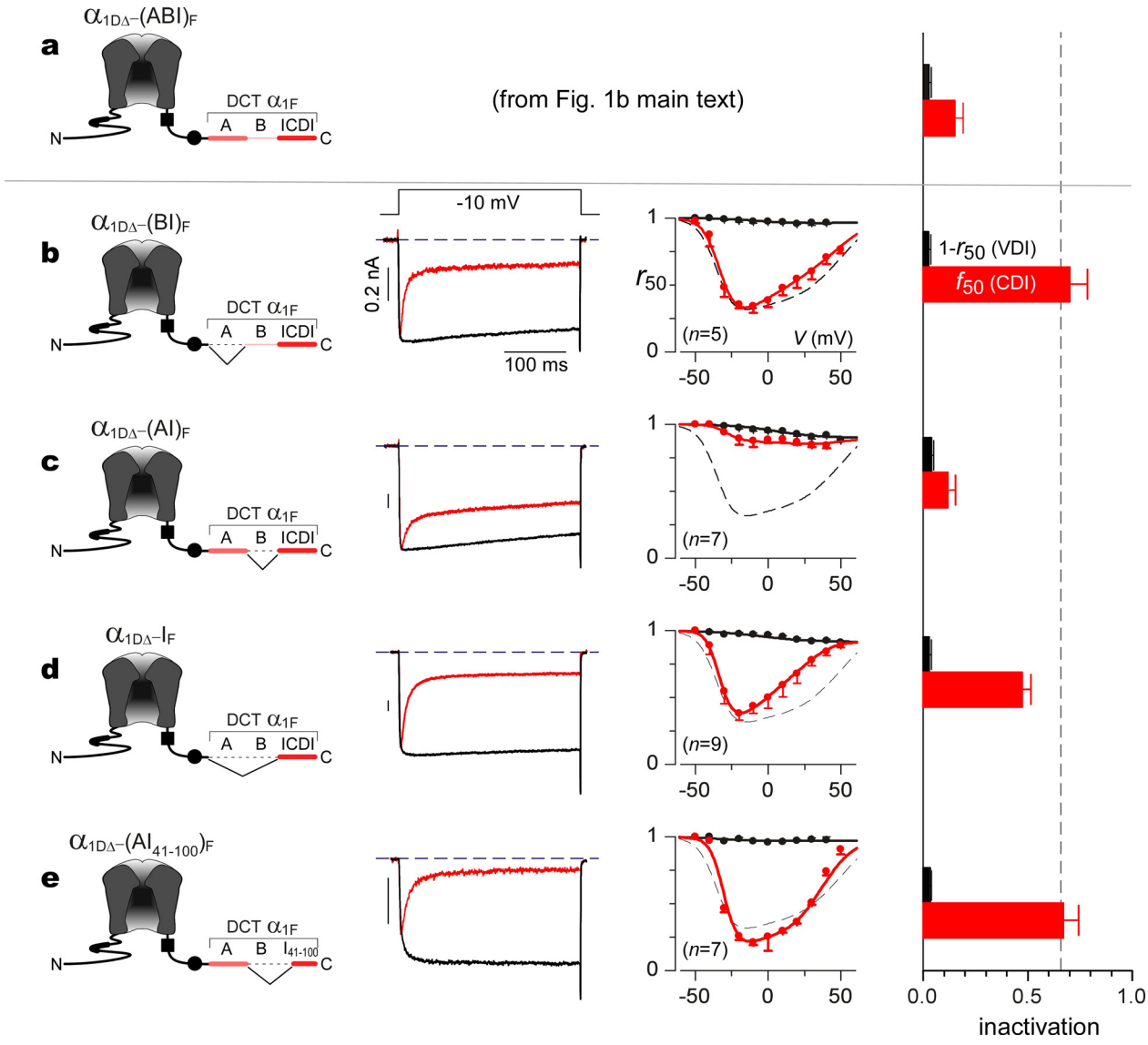

Fig. S1.4 Deletion analysis of the $\alpha_{1D\Delta}$-$(ABI)_F$ construct. Format as in main text Fig. 1 throughout this supplemental figure. **a,** Summary of CDI profile of $\alpha_{1D\Delta}$-$(ABI)_F$ construct, copied from main text Fig. 1b for reference. Bar graphs indicate strongly attenuated CDI, compared to that of core channels whose behavior follows the dashed curves. **b**, Deleting the A segment fully restores CDI. **c**, Deleting the B region fully maintains suppression of CDI by the remaining DCT elements. **d**, Deleting both A and B segments, leaving only the ICDI element, yields only a small decrease of CDI. **e**, Deleting the first 40 aa of the ICDI element in the construct of panel **c** (leaving `VALA...VHAL`) fully eliminates DCT function. Sequences in Fig. S1.1; QuikChange used to delete DCT portions, before non-directional cloning into a unique Xba I site.

1.5. Competitive versus strict allosteric mechanisms underlying DCT effects

There is an ongoing controversy concerning the mechanism underlying DCT effects. One proposed mechanism is the strict allosteric scheme diagrammed in Fig. S1.5a. Here, the ICDI module leaves apoCaM/channel binding unchanged, but the association of ICDI with an EF-hand-like module eliminates CDI transduction . Alternatively, in a competitive mechanism as shown in Fig. S1.5b, ICDI competes with apoCaM for binding near the channel IQ domain. CDI is thus inhibited by displacement of CaM from channels.

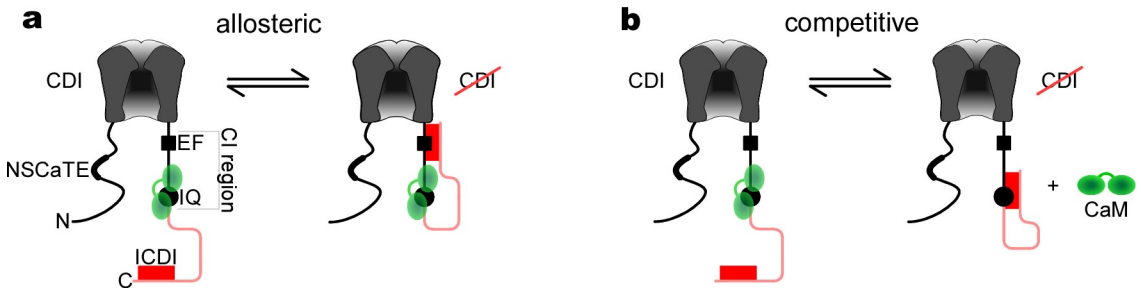

Fig. S1.5 Two proposed mechanisms underlying DCT effects. **a**, Strict allosteric mechanism. ICDI binding to EF-hand-like module does not perturb apoCaM binding to IQ domain, but instead eliminates transduction of CDI. **b**, Competitive inhibitory mechanism. ICDI competes with apoCaM for binding to IQ domain. Channels fail to undergo CDI because they altogether lack a preassociated apoCaM.

2. Additional data for Fig. 2

2.1. Detailed composition of FRET 2-hybrid constructs

For main text Figs. 2a through 2c, EYFP–PreIQ$_3$–IQ$_D$–A$_F$ contains the PreIQ$_3$–IQ$_D$ segment of the rat $\alpha_{1D\Delta}$ subunit (IKTEGNLEQANEELRAVIKKIWKKTSMKLLDQVVPPAGDDEVTVGKFYAFLIQ...GLVG) fused to the A segment of α_{1F} in Fig. S1.1. CFP–CaM$_{WT}$ is as published[3]. For main text Figs. 2d and 2e, CaM$_{WT}$ and CaM sponge (specifically, EYFP–PreIQ$_3$–IQ of α_{1C}) are also as published[3].

2.2. Additional FRET interactions of the ICDI element of α_{1F}

To confirm that the FRET interactions in main text Fig. 2c are representative of those pertaining to full-length CaV1.4 channels, Fig. S2.2a shows the FRET binding curve for the apoCaM preassociation domain of Ca$_V$1.4 (EYFP–PreIQ$_3$-IQ$_F$–A$_F$) with ECFP–ICDI$_F$. This curve is closely similar to that for interacting partners of the $\alpha_{1D\Delta}$–(ABI)$_F$ channel chimera in main text Fig. 2c, suggesting that this chimera is an appropriate proxy for full-length Ca$_V$1.4 behavior.

Structural modeling and electrophysiological analysis of Ca$_V$1.2 channel deletions/mutations indirectly suggest that segments homologous to the A and ICDI segments bind in these channels[7]. Moreover, single-metric FRET analysis of homologous A and ICDI segments in Ca$_V$1.3 channels also indirectly suggest that these segments interact A[8]. By contrast, our FRET 2-hybrid analysis below (Fig. S2.2b) directly indicates a lack of FRET interaction between A and ICDI segments of the DCT of Ca$_V$1.4 channels, over a wide range of free ICDI concentrations. Instead of direct interaction, the A region is important to permit the PreIQ$_3$-IQ domain to interact well with the ICDI region (not shown).

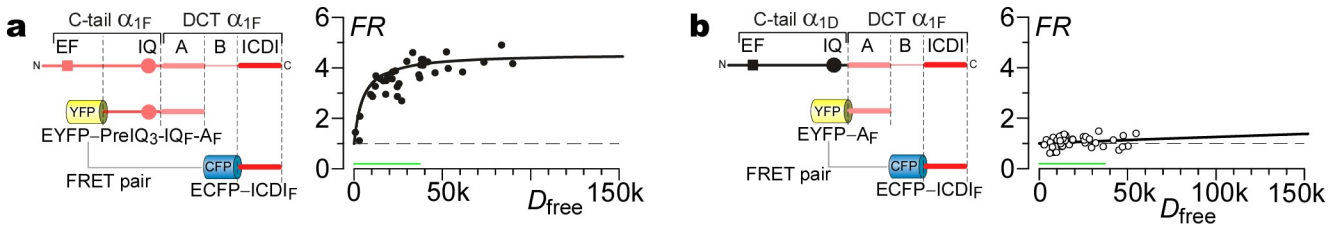

Fig. S2.2 **a**, FRET 2-hybrid binding curve for EYFP–PreIQ$_3$-IQ$_F$–A$_F$ and ECFP–ICDI$_F$, all derived from Ca$_V$1.4. **b**, A and ICDI elements of α_{1F} (main pore-forming subunit of Ca$_V$1.4 channels) fail to exhibit FRET interaction. Failure of data points to rise above unity indicates lack of appreciable FRET interaction. **a** and **b**, Format identical to that in main text Fig. 2a. Left, schematic of FRET partners used in experiment. Right, binding curve plotting *FR* metric of FRET (proportional to FRET efficiency) versus relative concentration of free ICDI species.

2.3. Overexpression of Ca^{2+} insensitive mutant CaMs with $\alpha_{1D\Delta}$-$(ABI)_F$ construct

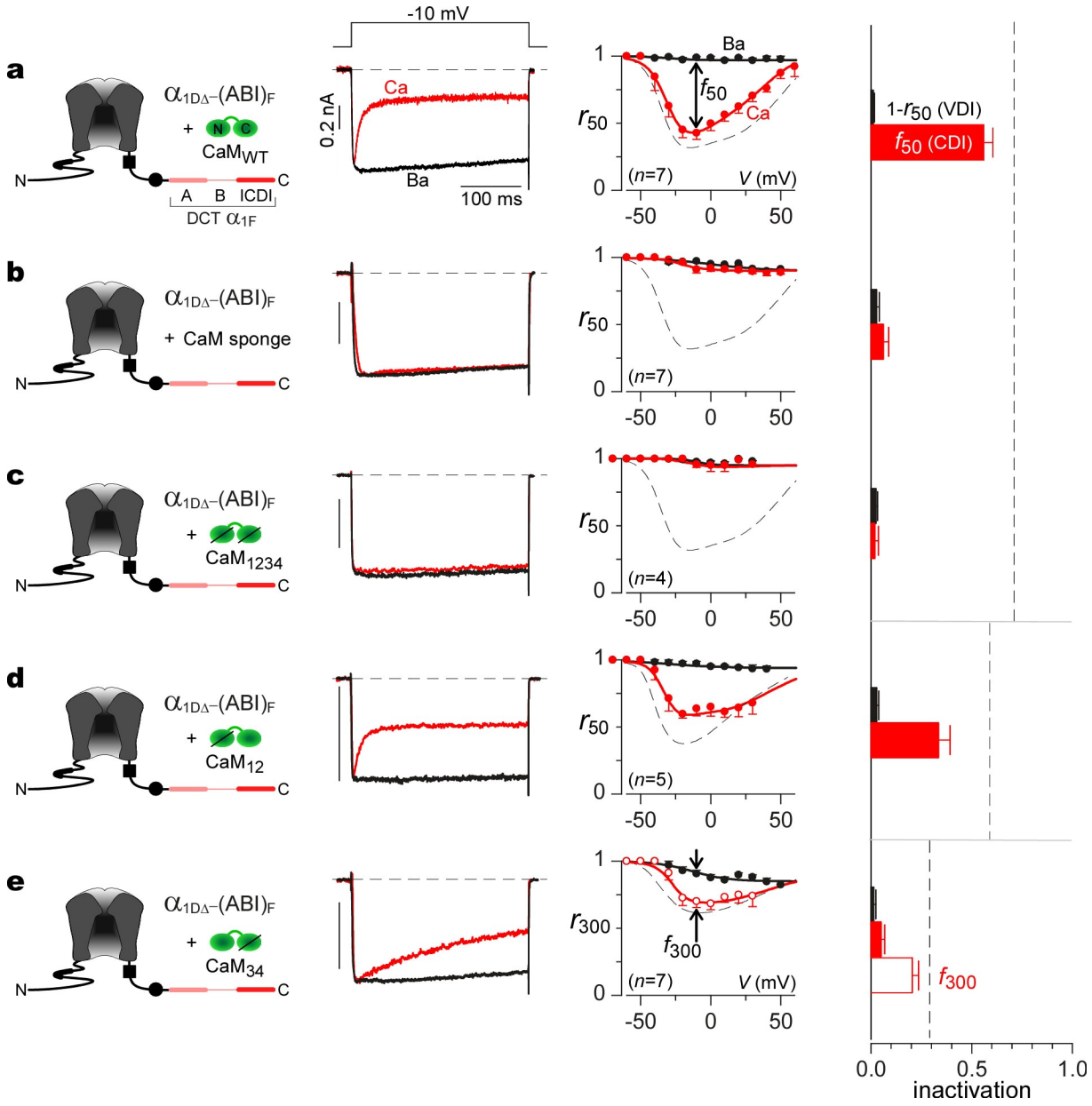

Fig. S2.3 Changes in the CDI of $\alpha_{1D\Delta}$-$(ABI)_F$ channels upon manipulating wild-type CaM levels, or overexpressing various Ca^{2+}-sensitive mutant CaM molecules[1]. Format as in main text Fig. 1, with addition of bar graph population summaries of VDI and CDI parameters at far right. **a**, **b**, Expanded analysis of main text Fig. 2d. **a**, Overexpressing wild-type CaM restores CDI almost to control levels (dashes). **b**, Chelating CaM with a CaM sponge peptide nearly eliminates CDI. **c**, Coexpression with CaM_{1234} eliminates all appreciable CDI. **d,** Coexpression with CaM_{12} largely restores a C-lobe form of CDI. Dashed curves show metrics for parallel experiments on $Ca_V1.3$ channels lacking a DCT[4]. **e,** Coexpression with CaM_{34} largely restores an N-lobe form of CDI. Dashed curves show metrics for parallel experiments on $Ca_V1.3$ channels lacking a DCT[4]. Additional 300-msec CDI metrics used here to facilitate characterization of slower N-lobe form of CDI.

Co-expressing the $\alpha_{1D\Delta}$-$(ABI)_F$ construct with an abundance of CaM and CaM sponges (Figs. S2.3a and S2.3b, respectively)—or with a plethora of various Ca^{2+}-sensitive mutant CaM molecules[1] (Figs. S2.3c through S2.3e)—all furnish another body of evidence that circumstantially supports a competitive inhibitory mechanism (Fig. S1.5b). For panels a and b, these data sets amplify the analysis shown in main text Fig. 2d. Alternatively, if we could fully repopulate channels with a specific form of mutant CaM under a competitive inhibitory mechanism (panels c through e), then the resulting CDI profile should adopt

that of channels that lack a DCT module and bear such mutant CaM molecules[4]. Indeed, this outcome is largely realized. When a CaM lacking Ca^{2+} binding to all four EF hands (CaM_{1234}) is coexpressed, CDI becomes essentially zero (Fig. S2.3c). When a CaM_{12} (Ca^{2+} binding only to C-lobe of CaM) is coexpressed, a mostly C-lobe form of CDI is observed (Fig. S2.3d). CDI metrics for C-lobe CDI in channels lacking a DCT are shown as dashed relations[4]. When CaM_{34} is coexpressed, a mostly N-lobe form of CDI is observed (Fig. S2.3e). Here, 300-msec CDI metrics are included, to resolve the slow N-lobe form of CDI with better precision. Dashed relations indicate the N-lobe CDI metrics from channels lacking a DCT element[4]. The close approximation of $\alpha_{1D\Delta}$-$(ABI)_F$ data with that of $Ca_V1.3$ lacking a DCT module circumstantially supports a competitive inhibitory mechanism.

3. Formulation of Equation 1 for competitive inhibitory mechanism in Fig. 3

3.1. Sequence of CaM sponges in Fig. 3b

Filled green symbol, rat neuromodulin IQ domain[6] (MAATKIQA**A**FRGHITRKKLKDEKKGASRGPYSIVSPKC, NP058891), with boldface S41A mutation to eliminate PKC site[6] ; open symbol, PreIQ3-IQ of α_{1C} as reported[3]; both without fluorophore.

3.2. *FR* to apoCaM relation

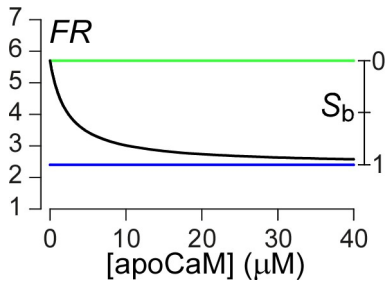

Fig. S3.2 Relation between FRET metric[3] *FR* and free apoCaM concentration, as given by the $BSCaM_{IQ}$ sensor.in HEK293 cells[6]. *FR* relates to the fractional binding of $BSCaM_{IQ}$ with apoCaM by the following equation: $S_b = (FR_{max} - FR) / (FR_{max} - FR_{min})$, where FR_{max} and FR_{min} values are given by green and blue line levels. Free apoCaM concentration is then determined from S_b via Eq. S4 below. Plotting these relations yields the black curve shown at left that relates *FR* to free apoCaM concentration.

3.3. Derivation in terms of $BSCaM_{IQ}$ sensor readouts

From previous analyses, we know that channels lacking a preassociated apoCaM fail to exhibit CDI[3,5]. Additionally, a competitive inhibitory mechanism postulates that once apoCaM preassociates with the channel to displace the competitive inhibitor (ICDI), the strength of CDI (f_{50}, as defined in main text Fig. 1a) should adopt the full value CDI_{max}, just as observed without inhibitor[9]. Accordingly, according to this model, the strength of CDI is

$$CDI = CDI_{max} \cdot F_{\text{bound-channel}} + 0 \cdot (1 - F_{\text{bound-channel}}) \tag{S1}$$

where $F_{\text{bound-channel}}$ is the fraction of channels to which apoCaM is pre-bound. Ca^{2+} binding to pre-bound apoCaM then drives conformational changes that invoke CDI. This equation also presumes that channels preassociated with apoCaM exhibit the same single-channel current amplitudes as do channels without CaM. These and other presumptions will ultimately be confirmed by full consistency with extensive data sets within the main text.

According to a competitive inhibitory mechanism, we can also postulate that

$$F_{\text{bound-channel}} = \frac{[\text{apoCaM}]}{[\text{apoCaM}] + K_{\text{d-channel-apparent}}} \tag{S2}$$

where [apoCaM] is the free concentration of apoCaM, and $K_{\text{d-channel-apparent}}$ is the apparent dissociation constant of the channel in the presence of a fixed concentration of inhibitor (as true with an ICDI element covalently linked to the channel complex). This equation exploits the facts that CaM exchanges slowly with Ca^{2+} channels over the course of ~30 minutes[10], and that our culture conditions and experiments maintain cells in the resting state where apoCaM predominates[3,11], except for brief activations of channel current in the presence of 5 mM intracellular EGTA (which maintains all but local Ca^{2+} concentration near zero). These periods of activation do not perturb $F_{\text{bound-channel}}$, as repeated cycles of activation fail to appreciably change CDI (see Eq. S1).

To link these equations to FRET sensor readings, we recall that the $BSCaM_{IQ}$ sensor gives direct measurements of [apoCaM] according to[6]

$$S_b = \frac{[\text{apoCaM}]}{[\text{apoCaM}] + K_{\text{d-sensor}}} \tag{S3}$$

where S_b is the fraction of sensor bound to apoCaM (readout from Fig. S3.2 and main text Fig. 3b), and $K_{\text{d-sensor}}$ is the dissociation constant of the sensor in HEK293 cells, determined to be 2.3 μM[6]. The accuracy of this description of the sensor is enhanced for several reasons. The $BSCaM_{IQ}$ sensor is sensitive almost exclusively to free apoCaM concentration (not Ca^{2+}/CaM), unless Ca^{2+} is elevated to far greater than 10 μM[6]. Readings of the sensor are taken in resting HEK293 cells (before whole-cell dialysis is begun), where the Ca^{2+} is certainly less than 10 μM. The whole-cell recording solution contains 5 mM EGTA to ensure near zero global Ca^{2+} upon dialysis, so that sensor readings do not change appreciably upon whole-cell recording and activation of currents. Also, the nearly constant FRET upon dialysis also suggests negligible CaM diffusion from cell to pipet over ~10 m recording.

As FRET measurements furnish a direct determination of S_b, as diagrammed in main text Fig. 3b, it is useful to convert Eq. S3 into a determination of [apoCaM] in terms of S_b.

$$[\text{apoCaM}] = K_{\text{d-sensor}} \cdot \frac{S_b}{1 - S_b} \tag{S4}$$

Substituting Eq. S4 into S2 yields

$$F_{\text{bound-channel}} = \frac{K_{\text{d-sensor}} \cdot \dfrac{S_b}{1 - S_b}}{K_{\text{d-sensor}} \cdot \dfrac{S_b}{1 - S_b} + K_{\text{d-channel-apparent}}} \tag{S5}$$

Substituting Eq. S5 into Eq. S1 then yields Eq. 1 in the main text.

3.4. Exemplar current traces for Figs. 3e through 3g

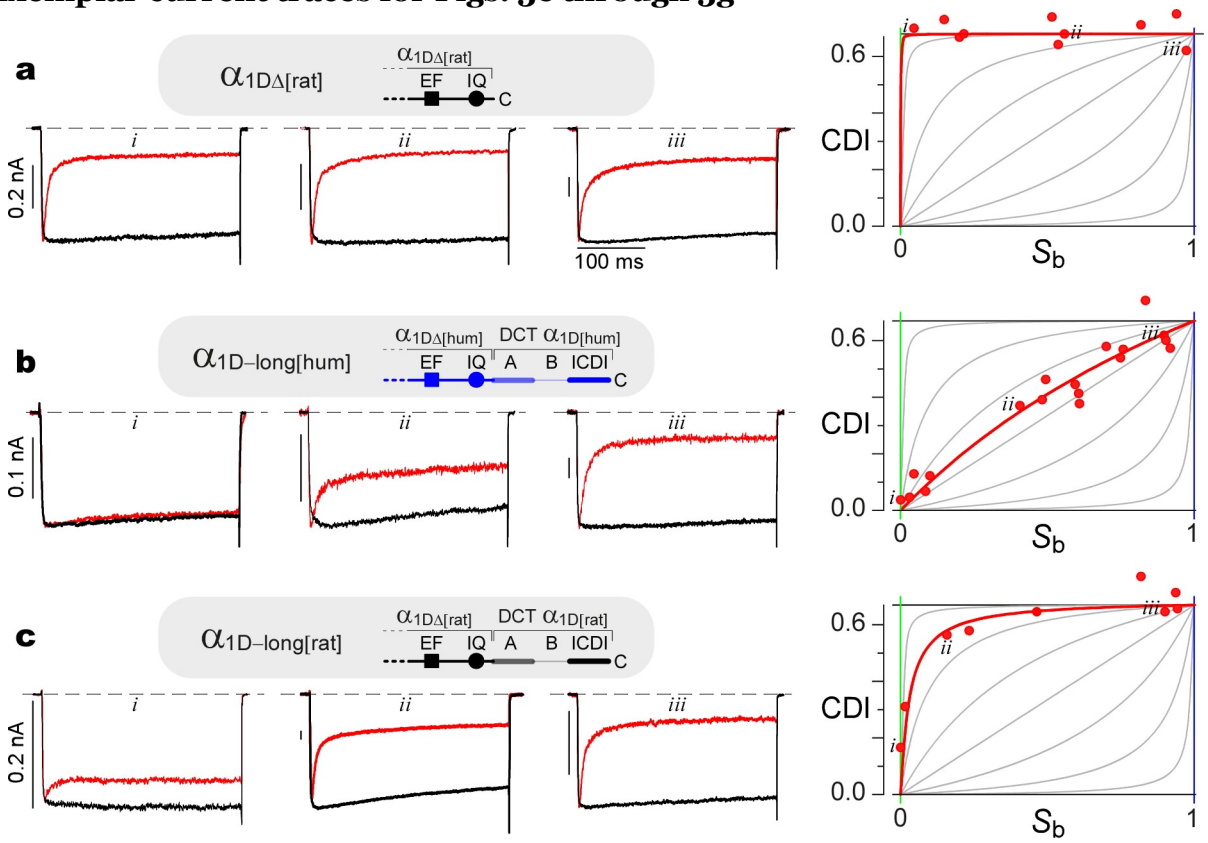

Fig. S3.4 Exemplar currents accompanying main text Figs. 3e, 3f, and 3g. **a**, Reproduction of main text Fig. 3e graph for $\alpha_{1D\Delta[rat]}$ (far right), now labelled with exemplar current labels (i – iii). The corresponding exemplar currents are displayed at left. **b**, Reproduction of main text Fig. 3f data for $\alpha_{1D–long[hum]}$ (far right); affiliated exemplar currents (left). Format as in **a**. **c**, Reproduction of main text Fig. 3g data for $\alpha_{1D–long[rat]}$ (far right); affiliated exemplar currents (left). Format as in **a**.

3.5. Single-residue switch explains differing ICDI functions of rat versus human $Ca_V1.3$

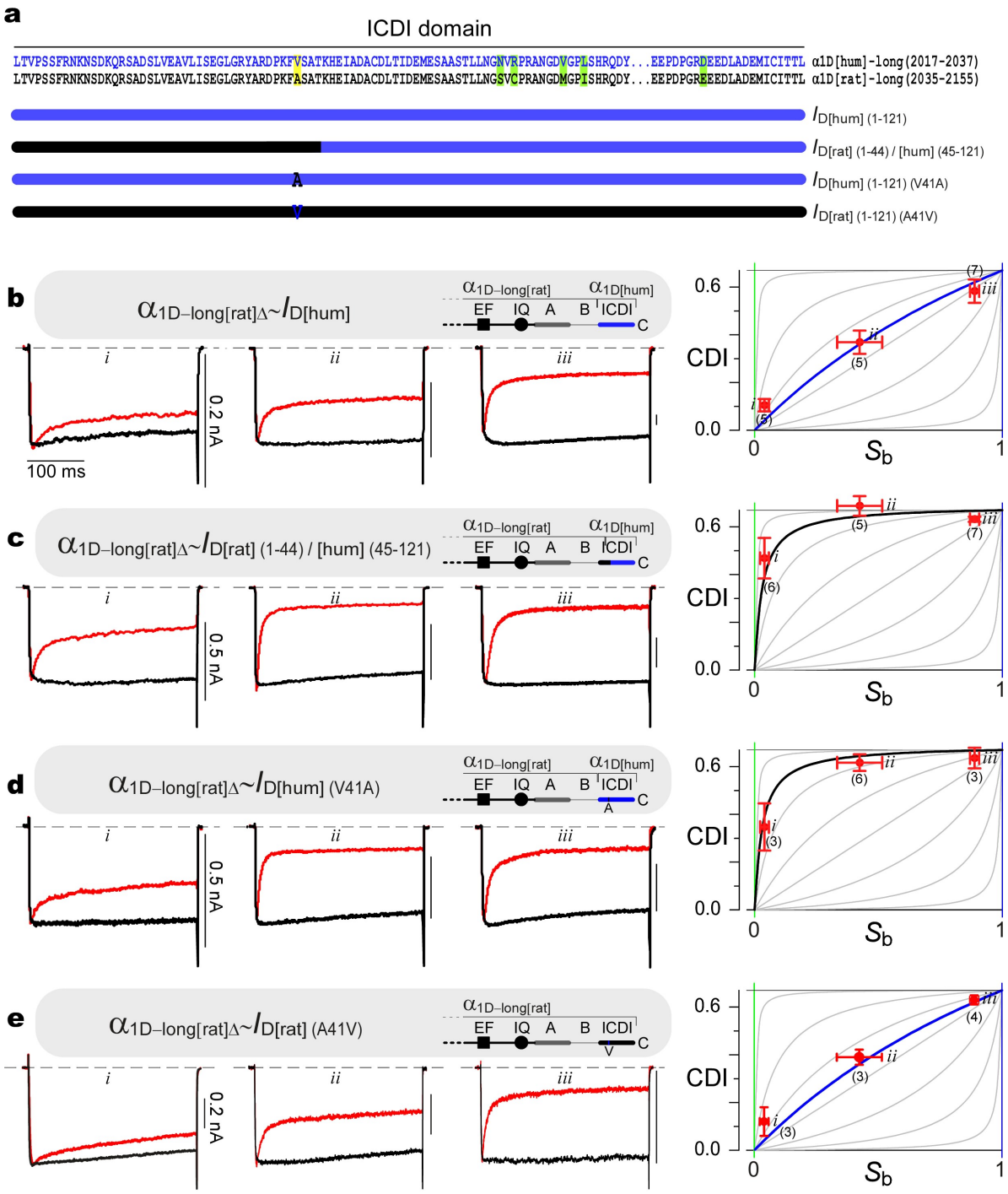

Fig. S3.5 Single residue differentially tunes long variants of human and rat $Ca_V1.3$. **a**, Amino-acid alignments of ICDI region for long variants of human and rat $Ca_V1.3$. Top, highlighted residues mark differences between variants; bottom, bars schematize engineered versions of ICDI to be substituted into $\alpha_{1D–long[rat]}$ below. An SS punctuates IQ/A and rat/human junctions in these constructs. **b**, *CDI*–S_b analysis for $\alpha_{1D–long[rat]\Delta}$~$I_{D[hum]}$ (human ICDI substituted into the long rat variant) converts the rat into human phenotype. **c**, *CDI*–S_b analysis for $\alpha_{1D–long[rat]\Delta}$~$I_{D[rat](1-44)/[hum](45-121)}$ (last 77 residues of human ICDI substituted into the rat variant) shows sparing of the rat profile, implicating functional dominance of first 44 residues in human ICDI. **d**, *CDI*–S_b analysis for $\alpha_{1D–long[rat]\Delta}$~$I_{D[hum](V41A)}$ (human ICDI with V41A mutation substituted into rat variant) spares the rat profile, identifying a valine-to-alanine switch at ICDI position 44 as critical to intra-species tuning of long $Ca_V1.3$ variants. **e**, *CDI*–S_b analysis for $\alpha_{1D–long[rat]\Delta}$~$I_{D[rat](A41V)}$ (rat ICDI with A41V mutation substituted into rat variant) confers the human profile, proving the valine-to-alanine switch at ICDI position 44 to be both necessary and sufficient for the intra-species tuning of long $Ca_V1.3$ variants.

Given that ICDI peptide interactions presumably underlie channel inhibitory tuning (main text Fig. 2c), we focused a search for critical residues within this locus. Upon substituting the human $Ca_V1.3$ ICDI element ($I_{D[hum](1-121)}$, Fig. S3.5a) into the long variant of rat $Ca_V1.3$ channels, the resulting channels exhibited a *CDI*–S_b profile approximating that of the long $Ca_V1.3$ variant of humans (Fig. S3.5b, blue curve from main text Fig. 3f), confirming functional dominance of ICDI. An abbreviated *CDI*–S_b analysis was employed to facilitate structure-function analysis (for details, see paragraph below). Upon reversion of the first 44 residues of the human ICDI into those of their rat counterpart ($I_{D[rat](1-44)\,/\,[hum](45-121)}$, Fig. S3.5a), the *CDI*–S_b profile resembled that of the long $Ca_V1.3$ variant of rat (Fig. S3.5c, black curve from main text Fig. 3g), demonstrating the critical nature of this initial segment. Close inspection of sequence within this zone (Fig. S3.5a) revealed a single valine (human) to alanine (rat) difference (yellow highlight). After point valine-to-alanine mutation of the human ICDI ($I_{D[hum](1-121)(V41A)}$, Fig. S3.5a), substitution of this element into the long variant of rat $Ca_V1.3$ channels retained the *CDI*–S_b profile of the long rat variant (Fig. S3.5d). Conversely, after point alanine-to-valine mutation of the rat ICDI ($I_{D[rat](1-121)(A41V)}$, Fig. S3.5a), substitution of this element into the long variant of rat $Ca_V1.3$ channels conferred the *CDI*–S_b profile of the long human variant (Fig. S3.5e). FRET assays of corresponding ICDI peptide and IQ domain binding showed directionally consistent changes in affinity (Supplemental Fig. S3.6 below). Hence, a single-residue switch gives rise to the differing inhibitory strengths of ICDI modules from rat and human $Ca_V1.3$.

Abbreviated *CDI*–S_b analysis. To facilitate rapid structure-function analysis, S_b in these experiments were determined in separate experiments from those used to determine CDI. The lowest S_b value was obtained from $\alpha_{1D-long[hum]}$ experiments wherein overexpression of $BSCaM_{IQ}$ was employed to chelate apoCaM (main text Fig. 3f, 5 cells). The intermediate S_b value was obtained from $\alpha_{1D\Delta}$–$(ABI)_F$ experiments without further apoCaM perturbation (main text Fig. 1b, 7 cells), projected through our highest resolution *CDI*–S_b relation (main text Fig. 3d). The highest S_b value was obtained from $\alpha_{1D-long[hum]}$ experiments wherein overexpression of CaM_{WT} was employed to elevate apoCaM (main text Fig. 3f, 4 cells).

FRET 2-hybrid peptide interaction assays (Supplemental Fig. S3.6) confirm directionally consistent changes in binding of $PreIQ_3$-IQ-A to ICDI peptides, corresponding to *CDI*–S_b data in Supplemental Figs. S3.5b and S3.5d.

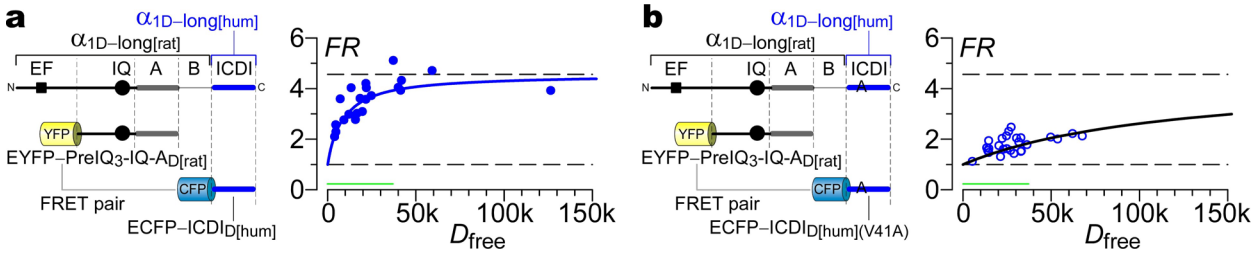

Fig. S3.6 FRET 2-hybrid analysis of peptide segments corresponding to Supplemental Figs. S3.5b, d. Format as in main text Fig. 2a, but without unlabelled neuromodulin IQ. **a**, YFP-tagged $PreIQ_3$-IQ-A segment of $\alpha_{1D-long[rat]}$ pitted against CFP-tagged ICDI segment of $\alpha_{1D-long[hum]}$. Binding curve data (symbols) conform to fit obtained from YFP-tagged $PreIQ_3$-IQ-A segment of $\alpha_{1D-long[hum]}$ pitted against CFP-tagged ICDI segment of $\alpha_{1D-long[hum]}$, reproduced from main text Fig. 4b (top). This outcome fits nicely with concordance of functional *CDI*–S_b data between $\alpha_{1D-long[rat]\Delta}$~$I_{D[hum]}$ (Fig. S3.5b) and $\alpha_{1D-long[hum]}$ (main text Fig. 3f). **b**, YFP-tagged $PreIQ_3$-IQ-A segment of $\alpha_{1D-long[rat]}$ pitted against CFP-tagged ICDI segment of $\alpha_{1D-long[hum](V41A)}$. Binding curve data (symbols) conform to fit obtained from YFP-tagged $PreIQ_3$-IQ-A segment of $\alpha_{1D-long[rat]}$ pitted against CFP-tagged ICDI segment of $\alpha_{1D-long[rat]}$, reproduced here from main text Fig. 4b (bottom). This outcome concurs with agreement of functional *CDI*–S_b data of $\alpha_{1D-long[rat]\Delta}$~$I_{D[hum](V41A)}$ (Fig. S3.5d) and $\alpha_{1D-long[rat]}$ (main text Fig. 3g).

4. Additional derivations and data for Fig. 4

4.1. Derivation of Eq. 2 for classic competitive inhibitory mechanism

A further standard result for competitive inhibitory mechanisms is that[9,12]

$$K_{\text{d-enzyme-apparent}} = K_{\text{d-enzyme-actual}}(1+[\text{I}]/K_{\text{I}}) \tag{S6}$$

where $K_{\text{d-enzyme-apparent}}$ is the apparent dissociation constant of substrate from the enzyme (factoring in the effect of a competitive inhibitor), [I] is the concentration of the competitive inhibitor, and K_{I} is the dissociation constant of inhibitor from the enzyme (in the absence of substrate). This additional property of classic competitive inhibition offers constraints beyond those of main text Eq. 1, and furnishes further means to exclude other inhibitory mechanisms[9,12]. For example, non-competitive mechanisms feature an unchanging $K_{\text{d-enzyme-apparent}}$ independent of [I], whereas uncompetitive mechanisms exhibit a changing $K_{\text{d-enzyme-apparent}}$ with directionally opposite dependence upon [I]. Casting Eq. S6 in terms of our particular DCT/channel mechanism yields Eq. 2 within the main text.

What of the further significance of Eq. 2 for our mechanistic deductions? Already plausible from the sufficiency of main text Eq. 1 is that the holochannel exhibits a competitive inhibitory mechanism. Beyond this, experimental evaluation of Eq. 2 furnishes an extraordinary test of whether ICDI competition with apoCaM for the PreIQ3-IQ segment comprises the actual suite of molecular interactions that underlie holochannel competition. This is because $K_{\text{d-channel-apparent}}$ comes from holochannel measurements, whereas $K_{\text{d-FRET-peptide}}$ comes from FRET 2-hybrid peptide data. If Eq. 2 is not satisfied, then ICDI competition with apoCaM for the PreIQ3-IQ segment is epiphenomenological, and does not actually underlie holochannel competition. Hence, the substantiation of Eq. 2 in main text Fig. 4c furnishes important support that we have correctly identified the actual molecular interactions underlying holochannel competition. This is a significant result given the multiplicity of potential CaM binding segments on voltage-gated channels[2,13]. Our overall strategy should prove generally useful for dissecting mechanism in macromolecules with several regulatory sites.

A final set of insights comes from the regression analysis of main text Eq. 2 (main text Fig. 4c). The *y*-intercept and slope yield molecular parameters that are difficult to deduce by other means. The intercept yields the affinity of the core channel for apoCaM in the absence of inhibitor (~10 nM), and the slope can then be used to calculate the local concentration (at the IQ site) of the intramolecular ICDI element (~15 μM). These values might be 'effective' parameters if there is local enrichment of apoCaM concentration near channels[14], akin to partition coefficient alteration of permeant ion concentration at the membrane interface of GHK channels[15].

4.2. Excluding even a mixed allosteric-competitive inhibitory scheme via Eq. 2

A highly nuanced allosteric scheme, termed a mixed allosteric-competitive inhibitory mechanism, is the most difficult to exclude[9,12] (Fig. S4.2a). Here, apoCaM and ICDI elements do not bind to the same channel sites; however, the binding of ICDI renders apoCaM binding to the channel more difficult. In other words, the binding of apoCaM to state 2 is easier than to state 1 ($K_{\text{d}}' > K_{\text{d}}$). Channels lacking apoCaM exhibit no CDI (states 1 and 2); channels bound only to apoCaM and not ICDI exhibit full strength $CDI_{\max}$ (state 3); and channel bound to both apoCaM and ICDI (state 4) can also exhibit CDI with strength $f \cdot CDI_{\max}$ ($0 \le f \le 1$). Because overexpression of CaM fully recovers CDI to a common $CDI_{\max}$ level, f would have to be equal to unity in our considerations. In this case, the mixed scheme will behave entirely according to main text Eq. 1, rendering this nuanced allosteric mechanism most difficult to exclude. Specifically,

$$CDI = CDI_{\max} \cdot \frac{[\text{apoCaM}]}{[\text{apoCaM}] + K_{\text{d-channel-apparent}}} \tag{S7}$$

just as in the case of the classic competitive inhibitory mechanism (Eqs. S1 and S2). The saving grace comes with consideration of the specific dependence of $K_{\text{d-channel-apparent}}$ upon [I]:

$$K_{\text{d-channel-apparent}} = K_{\text{d-channel}} \cdot \frac{(1+[\text{I}]/K_{\text{I}})}{(1+[\text{I}]/K_{\text{X}})} = K_{\text{d-channel}} \cdot \frac{(1+[\text{I}]/K_{\text{I}})}{(1+[\text{I}]/(\alpha \cdot K_{\text{I}}))} \quad \text{(S8)}$$

where $K_{\text{d-channel}}$ is the dissociation constant of apoCaM from the channel in the absence of inhibitor (from states 3 to 2 in Fig. S4.2a); K_{I} is the dissociation constant of ICDI inhibitor from the channel in the absence of apoCaM (from states 1 to 2 in Fig. S4.2a); and K_{X} is the dissociation constant of ICDI inhibitor from the channel with apoCaM bound (from states 4 to 3 in Fig. S4.2a). For convenience, we

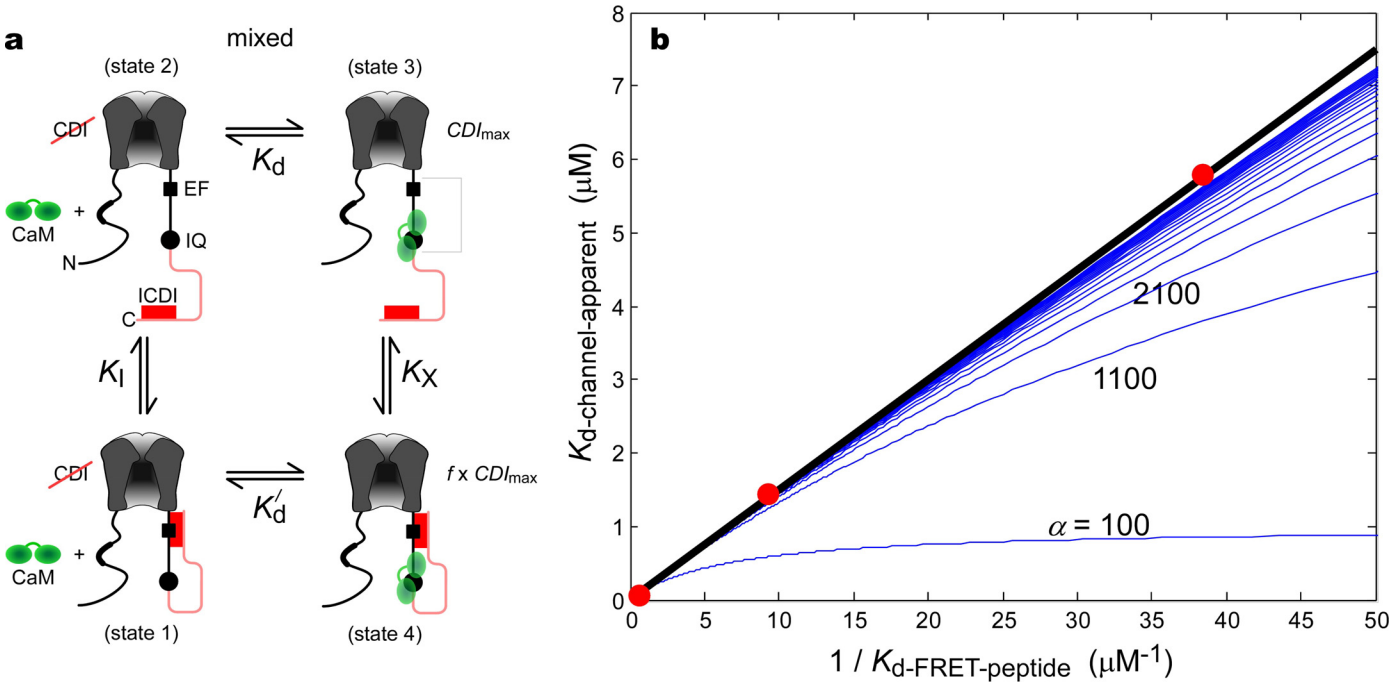

Fig. S4.2 Analysis affiliated with main text Eq. 2 excludes mixed allosteric-competitive mechanism. **a**, Schematic diagram of mixed allosteric-competitive mechanism. **b**, Fit of Eq. S8 to data of main Fig. 4c. α parameter (where $K_X = \alpha \cdot K_I$) must be greater than 1100 to fit data, thereby excluding mixed model, for all practical purposes.

set $K_X = \alpha \cdot K_I$, where $\alpha > 1$ implies that occupancy of state 4 is less likely than state 1. If α is sufficiently larger than 1, then we recover a classic competitive inhibitory mechanism (Eq. S8 becomes main text Eq. 2). Since $K_I = K_{\text{d-FRET-peptide}}$, we can fit the data in main text Fig. 4c with Eq. S8 to estimate the value of α. We use $K_{\text{d-channel}} \sim 10$ nM and $[\text{I}] \sim 15$ μM, as obtained from linear regression analysis of Eq. 2 to data in main text Fig. 4c, because the y-intercept an initial slope of Eq. S8 would be the same. Fig. S4.2b shows fits of Eq. S8 (blue curves) to data (red symbols and linear fit in black reproduced from main text Fig. 4c). The most saturating blue curve is obtained with $\alpha = 100$, and subsequent curves utilize $\alpha = 1100, 2100, 3100 \ldots$ (as labeled). Even a conservative estimate indicates that α is certainly greater than 1100; this large value argues that, for all practical purposes, a classic competitive inhibitory mechanism holds true. This conclusion illustrates a final and powerful use of the analysis affiliated with main text Eq. 2 (main text Fig. 4c).

4.3. Neuromodulin coexpression experiments in main text Fig. 4e

In main text Fig. 4e (far right), we coexpressed the long variant of human $\text{Ca}_\text{V}1.3$ channels with rat neuromodulin (NP058891), wherein the IQ domain was engineered to avoid PKC variability via for S41A mutation (as in Supplemental 3.1). As a control, we also coexpressed an S41D mutation of rat neuromodulin that altogether eliminates apoCaM binding to neuromodulin. Channel CDI in this control ($f_{50} = 0.41 \pm 0.04$, $n = 5$) was no different than for channels expressed alone without neuromodulin (main text Fig. 4e, middle), confirming that the neuromodulin effect (main text Fig. 4e, far right) was indeed via buffering of apoCaM.

5. Supplemental information references

1. C. D. DeMaria, T. W. Soong, B. A. Alseikhan et al., *Nature* **411** (6836), 484 (2001).
2. I.E. Dick, M.R. Tadross, H. Liang et al., *Nature* **451**, 830 (2008).
3. M. G. Erickson, H. Liang, M. X. Mori et al., *Neuron* **39** (1), 97 (2003).
4. P. S. Yang, B. A. Alseikhan, H. Hiel et al., *J. Neurosci.* **26** (42), 10677 (2006).
5. H. Liang, C. D. DeMaria, M. G. Erickson et al., *Neuron* **39** (6), 951 (2003).
6. D. J. Black, J. Leonard, and A. Persechini, *Biochemistry* **45**, 6987 (2006).
7. J.T. Hulme, V. Yarov-Yarovoy, T.W. Lin et al., *J. Physiol. (Lond.)* **576**, 87 (2006).
8. A. Singh, M. Gebhart, R. Fritsch et al., *The Journal of biological chemistry* **283** (30), 20733 (2008).
9. C.R. Cantor and P.R. Schimmel, *Biophysical Chemistry: The behavior of biological macromolecules* 11 ed. (Macmillan, 1980).
10. D. Chaudhuri, B. A. Alseikhan, S. Y. Chang et al., *J. Neurosci.* **25** (36), 8282 (2005).
11. M. G. Erickson, B. A. Alseikhan, B. Z. Peterson et al., *Neuron* **31** (6), 973 (2001).
12. A.L. Lehninger, D.L. Nelson, and M.M. Cox, *Principles of biochemistry*, 4 ed. (Macmillan, 2005).
13. K. Dunlap, *J. Gen. Physiol.* **129** (5), 379 (2007); J. Kim, S. Ghosh, D. A. Nunziato et al., *Neuron* **41** (5), 745 (2004); G. S. Pitt, R. D. Zuhlke, A. Hudmon et al., *The Journal of biological chemistry* **276** (33), 30794 (2001); L. Xiong, Q. K. Kleerekoper, R. He et al., *The Journal of biological chemistry* **280** (8), 7070 (2005).
14. M. X. Mori, M. G. Erickson, and D. T. Yue, *Science* **304** (5669), 432 (2004).
15. B. Hille, *Ionic channels of excitable membranes*. (Sinauer Associates, Sunderland, MA, 1984).